WIRELESS POWER TRANSFER TO BATTERYLESS SENSORS USING MAGNETIC BLIND BEAMFORMING

by

Albert Aninagyei Ofori

B.Sc., July 2017, Kwame Nkrumah University of Science and Technology

A Thesis Submitted to the Faculty of
Norfolk State University in Fulfillment of the
Requirements for the Degree of

MASTER OF SCIENCE

ELECTRONICS ENGINEERING

NORFOLK STATE UNIVERSITY

November, 2021

Approved by:

_____

Dr. Hongzhi Guo (Advisor)

_____

Dr. Sacharia Albin (Member)

_____

Dr. Makarand Deo (Member)

ABSTRACT

WIRELESS POWER TRANSFER TO BATTERYLESS SENSORS

USING MAGNETIC BLIND BEAMFORMING

Albert Aninagyei Ofori
Norfolk State University, 2021
Advisor: Dr. Hongzhi Guo

Wireless sensors have vast applications in precision agriculture, underground tunnel sensing, body implants, and many others. As advancements in technology occur, these sensors can be made smaller and less intrusive, thereby making them more convenient for use in various media. One limitation that hampers efforts to achieve portability is batteries. Active sensors still require batteries which tend to be heavy, bulky, and potentially hazardous. Tiny batteryless sensors are desirable since they create negligible impacts on the operation of the system being monitored or the surrounding environment. Wireless energy transfer for batteryless sensors is challenging since they cannot cooperate with the charger due to their passive default state. In this thesis, a Magnetic Blind Beamforming (MagBB) algorithm is developed for wireless energy transfer for batteryless sensors in inhomogeneous media. Batteryless sensors with randomly orientated coils may experience significant orientation losses and they may not receive any energy from the charger. MagBB uses a set of optimized current vectors to generate rotating magnetic fields which can ensure that coils on batteryless sensors with arbitrary orientations can receive sufficient voltages for charging. It does not require any information regarding the batteryless sensor's coil orientation or location. The efficiency of MagBB is proven by extensive numerical simulations using a minimum of 3 mutually perpendicular current vectors up to 32 current vectors. A proof-of-concept prototype is then designed and analyzed. The effect of an inhomogeneous medium on Near-Field

Communication is also explored and proven to be negligible through experimentation.

ACKNOWLEDGEMENTS

I thank the Lord Almighty for His abundant grace since from the beginning of this program. My deepest appreciation goes out to my advisor Dr. Hongzhi Guo for his immense support, and my thesis committee members Dr. Sacharia Albin and Dr. Makarand Deo for their guidance throughout my studies, and during the process of my thesis.

Finally, I wish to acknowledge Prof. and Mrs. Ofori, who have been of great support as far as I can remember.

This study was support by the National Science Foundation (NSF) under grant number CNS1947748.

TABLE OF CONTENTS

LIST OF FIGURES

LIST OF TABLES

LIST OF ABBREVIATIONS

UHF	**U**ltra **H**igh **F**requency
RFID	**R**adio **F**requency **ID**entification
CDF	**C**ummulative **D**istribution **F**unction
MI	**M**agnetic **I**nduction
SDR	**S**emi-**D**efinite **R**elaxation
MOSFET	**M**etal **O**xide **S**emiconductor **F**ield **E**ffect **T**ransistor
MagBB	**Mag**netic **B**lind **B**eamforming
FPGA	**F**ield **P**rogrammable **G**ate **A**rray

1 INTRODUCTION

1.1 Background

Most automated systems today have one very salient component; a monitoring system. The presence and efficacy of such a system continuously measures and stores data based on which various decisions are made. Wireless sensors play an important role in precision agriculture. It can be used to collect information such as light intensity and leaf color. More recently, underground wireless sensors are also introduced to precision agriculture to monitor soil nutrition and moisture (Dong, Vuran, and Irmak, 2013; Vuran et al., 2018). An automated irrigation system will only be triggered when soil moisture falls below a certain predetermined threshold. The soil moisture would have to be periodically monitored and communicated to a central system using sensors. This system would then compare it with the threshold and send a command to actuate the irrigation pump. Monitoring systems are also important in describing various parameters in an environment, based on which studies and inferences can be drawn. The most salient components of a monitoring system consists of the sensors that are used to convert various parametric values to electronic data which can be further processed to yield meaningful information. For instance, in deep-tissue networking, sensors are implanted in the body which can measure health critical values such as blood sugar, based on which one's health can be reliably monitored. In agricultural applications, data such as temperature, salinity, humidity and the like can be studied to determine, for instance, how suitable the soil is for a specific crop, or how its parameters change during various seasons of the year. Today's wireless sensors are bulky and expensive, which is not suitable for large-scale wireless sensor networks. Hence, wireless sensors are used sparsely on farms.

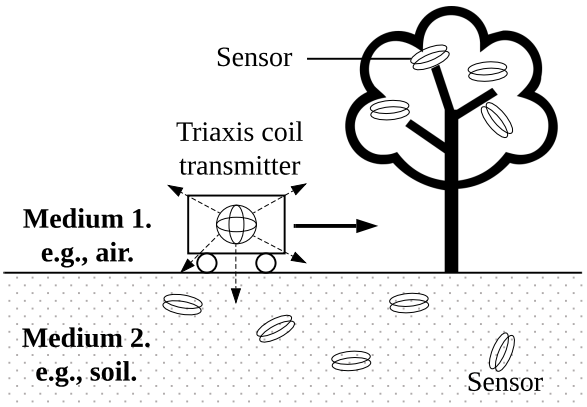

FIGURE 1.1: Illustration of a tri-axis coil in a moving robot being used to charge multiple batteryless sensors with tiny unidirectional coils.

However, as sensor technology improves, sensors can be made smaller and less intrusive thereby making them more suitable, especially for in-vivo applications.(Maselli et al., 2019; Ma et al., 2018) One limiting factor to the balance between longevity and portability of sensors, is battery size. Since sensors require power in order to wirelessly communicate information, and sometimes to pre-process the measured data for transmission, there can be no compromises on required power in favour of portability. Batteries are inconvenient in applications where sensors are not easily accessible as having to replace batteries, for instance, in an underground sensor would require precise knowledge of the sensor location and having to dig it up each time. The situation appears even more complicated when dealing with biosensors. This has necessitated the need for wireless power transfer so that sensors can work as batteryless devices which transmit the necessary information only when charged up.

Thus, tiny batteryless sensors are desirable. For example, batteryless sensors can be deployed aboveground and underground to monitor various parameters regarding plant health, as shown in Fig. 1.1. Since these sensors are small and low-cost, they do not require precise deployment, which is more convenient compared with traditional sensors.

Batteryless sensors rely on wireless energy transfer to support their normal operation. As shown in Fig. 1.1, a mobile wireless charger is used to wirelessly charge batteryless sensors. Since sensors are randomly located surrounding a plant, their

orientations and locations are unknown. Also, the plant growth is a dynamic process, previous information of sensor locations and orientations may not be useful.

Existing applications of wireless power transfer calculate a channel model based on which the power transfer implementation takes into account how the transmitted signal is altered by noise and the nature of the channel.

The channel estimation approach, however, is only ideal for active sensors which can provide channel information feedback to the charger (Jadidian and Katabi, 2014). In an uncontrolled and relatively dynamic environment in which the location of a sensor might change, or its orientation in space might be altered by various factors, the channel model approach might prove unreliable since the receiver parameters cannot be accurately determined using this method. In such a system, blind beamforming becomes a good method of overcoming such unpredictable circumstances. Using an efficient blind beamforming implementation, signals can be added constructively at the receiver without the knowledge of channel status information.

Magnetic induction is used because its operating frequency is in the HF band which demonstrates a long skin depth. In this case, if the communication range is much shorter than the wavelength, the impact of the soil-air boundary can be neglected (Guo, 2020) and, thus, we can consider the environment as a homogeneous medium. The mobile charger employs a tri-axis coil with three mutually perpendicular unidirectional coils. By optimally controlling the currents of the tri-axis coil, we can create magnetic fields in any direction. The main contribution of this study are detailed as follows

- A Magnetic Blind Beamforming (MagBB) algorithm is designed to rotate the magnetic field at a certain point to ensure that an arbitrarily orientated coil can receive sufficient power to charge the batteryless sensor.
- The performance of the algorithm s numerically evaluated and the impact of vector quantity and distance are analyzed.

- An experimental prototype is designed to implement the algorithm and practically confirm theoretically simulated behaviour.

2 RESEARCH CHALLENGES AND RELATED WORK

2.1 Research Challenges

The wireless energy transfer for batteryless sensors in inhomogeneous media is challenging due to the following reasons:

- The source of power used should be capable of simultaneously charging more than one underground device irrespective of their location or orientation in a three-dimensional space. In a system with more than one sensor, the power source should be capable of adequate power delivery to all sensors in the system.

- **Threshold voltage.** Typical energy harvesting circuits use a full-wave bridge rectifier (Ma et al., 2018) which consists of diodes to convert the induced AC voltages to DC voltages. Since diodes have a threshold voltage v_{th}, lower than which the circuit cannot harvest any energy. The typical v_{th} is around 200 mV which is hard to obtain when the distance between a charger and a sensor is large. Moreover, considering the tiny size of the batteryless sensor, the antenna is not efficient in receiving energy due to its low profile.

- **Unknown coil/receiver information.** Since a batteryless sensor does not store any energy, it cannot perform channel estimation for wireless energy transfer. Without the channel status information, efficient beamforming cannot be implemented. Thus, the wireless charger has no information about the receiver. There is no accurate method to determine the exact location of the sensors , and their respective channels, without having to probably physically ascertain their position and orientation.

- **Random coil/receiver location and orientation.** In an uncontrolled and relatively dynamic environment, the location of a sensor might change, or its antenna orientation in space might be altered by various factors. Even though sensors may be placed at specific, documented locations in the soil, the potentially dynamic nature of the internal soil environment can alter the exact location of a sensor over time. The growth of plants and the consequent penetration of their roots into the soil, for instance, has the potential to displace underground sensors to an unpredictable degree. Moreover, other uncontrollable phenomena such as erosion and seasonal changes in moisture can result in remarkable variations in communication channel conditions and the expected attenuation.

- **Inhomogeneous environment.** The wireless signal propagation is hard to predict due to the inhomogeneous environment, which may require complex beamforming algorithms. However, it is not trivial to map the environment and predict signal propagation. For instance in precision agriculture, the introduction of an underground system adds an additional consideration of a medium with different dielectric properties. For communication or power transfer in the electromagnetic range, a wave would experience a high level of attenuation and scattering in such a medium. Moreover, a medium like soil is non-uniform and also susceptible changes in periodic changes in parameters such as soil moisture content. This can further affect the channel properties and power transfer efficiency. It is therefore imperative to study and account for the practical effect of the communication channel.

The above challenges also arise individually in many other related works.

2.2 Related Work

In (Ma et al., 2018), the threshold voltage issue was addressed using blind beamforming analogous to the multipath fading in terrestrial environments. The UHF signals are used to power batteryless RFID sensors. However, UHF applications have been identified to have caveats of their own in inhomogeneous settings. Although higher frequency can extend communications range in the air when there is a direct line of sight between the transmitter and receiver, UHF communications have been identified to be highly susceptible to high attenuation and reflection in underground systems where there are obstructions between the source and destination as considered in this paper. This also greatly limits the communication range in these environments. This is emphasized in (Matsur et al., 2017) where a 2 m x 1 m x 1 m antenna is made for high accuracy sensing of potentially fast-moving traffic irrespective of vehicle positioning on the road. This antenna makes use of the HF (High-Frequency band) RFID standard at 13.56 MHz. The large width requirement of the antenna to cover the majority of the car lane to ensure a high level of accuracy also suggests proper alignment requirements for an adequately strong signal.

In (Yedavalli et al., 2017; Chen et al., 2016), adaptive blind beamforming is used for a multiantenna RFID reader. The RFID tag provides feedback signals to the reader to adaptively change the beamforming vectors. In this research, the batteryless sensors do not have the capability to provide any feedback due to the lack of sufficient energy. Therefore, a more low-power solution would be required. Magnetic induction with long-wavelength signals can efficiently penetrate through dense media due to the constant field conditions in the near-field. This has been used for wireless communication in extreme environments (Kisseleff, Akyildiz, and Gerstacker, 2014; Morag et al., 2019; Guo, Sun, and Wang, 2017; Guo and Sun, 2014). Also, the magnetic induction for wireless energy transfer has been widely accepted and the recently developed magnetic beamforming can significantly improve its efficiency (Jadidian and Katabi, 2014; Yang, Moghadam, and Zhang, 2017; Zhao et al.,

2020) using various mechanisms such as magnetic waveguide (Sun and Akyildiz, 2010; Tan, Sun, and Akyildiz, 2015) to extend the range with no additional energy requirement. However, with multiple batteryless sensors in a dynamic harsh environment, it becomes extremely complicated to deploy a magnetic waveguide to optimize charging efficiency from a single transmitter. Moreover, a wider communication range has been achieved by modelling the magnetic field characteristics of 3 mutually perpendicular coils in an underwater environment. By numerically deriving a simplified model characterizing the resultant magnetic field using vector spherical wave equations, a more reliable transmitter is developed and its accuracy is confirmed through simulation.(Guo, Sun, and Wang, 2015a) A combination of extended range and spatial diversity is also applied in (Guo and Sun, 2014) for communication in an oil reservoir setting. MagBB uses magnetic fields without knowing any information regarding the receiving coil, which is fundamentally different from existing solutions.

3 MODEL AND ALGORITHM DESIGN

In this section, we introduce the tri-axis coil model first. Then, we design a magnetic beamforming algorithm using current vectors. After that, we provide analytical analyses of the proposed algorithm and compare it with low-complexity solutions. Since we use long-wavelength magnetic induction signals, in the following we neglect the inhomogeneity of the environment and consider the sensors are located in homogeneous air medium. Also, due to the limited space of a batteryless sensor, it can only use a tiny unidirectional coil as the antenna.

3.1 Near-Field Communication

Before we proceed to design the communication system, a decision needs to be made on the most suitable power transfer methodology. In this case, the effects of the underground environment must be studied in order to formulate a practical idea of the channel attenuation characteristics based on the mode of communication, and how this affects our communication range. This knowledge can then be factored into various components of the model design in order to be as circumspect as possible and produce a robust algorithm. The dynamic nature of the inhomogeneous environment being studied is subject to change. Taking soil in an Air-to-Soil communication for instance, various changes in the internal ecosystem of the soil due to seasonal changes, erosion and the like can result in variations in the soil physical and electrical properties of the communication channel, for instance, the dielectric nature of the channel of communication. An ultra high frequency wave (UHF) would experience very high attenuation in such a medium. Moreover, due to the short wavelength, the range of communication will be very limited due to the high space loss experienced as the wavelength bears a logarithmically inverse

proportionality to the space loss. The propagating wave that would effectuate the power transfer to a receiver as we venture out of the near-field would experience great scattering in such a communication system. On the contrary, Near-Field Communication (NFC), as the name suggests would make use of magnetic induction which will mainly take place in the near field. The relatively lower frequency and longer wavelength, and therefore, lower space loss will make it more resilient in the underground medium. There is therefore limited scattering when magnetic induction is employed, thereby making it more suitable for the near-field communication as it is obviously less susceptible to in an inhomogeneous setting, and the more dominant near-field region extends the range of reliable communication.

3.1.1 Experimental Procedure

In order to fully comprehend the behaviour of NFC in an underground setting, experimental measurements were taken on a farm owned by Hampton Roads Agricultural Research and Extension Center, Virginia Beach, USA on December 3, 2020. As shown in Fig. 3.1A, an arduino Due in conjunction is interfaced with and Adafruit PN532 NFC breakout board and this assembly serves as the transmitter. This operates at 13.56 MHz and operates according to the ISO 14443 standard. The receiver is an 2-turn RF Solutions ANT- 1356M coil with a resonant frequency at 13.56 MHz. It has 6.5 cm diameter. In order to measure the received power, an Agilent N9320A spectrum analyzer is employed in measuring the said values via a BNC connection interface to the receiver. Three location measurements were taken in order to draw a comparison between power transfer across different media;

- **Air2Air channel:** Here, both the transmitter and receiver are located 10 cm above the soil.
- **Air2Soil channel:** The transmitter is located 10 cm above the soil surface and the receiver is located 30 cm below the soil.

- **Soil2Air channel:** The transmitter is buried 30 cm below the soil and the receiver is placed 10 cm above the soil surface.

The lateral distance between the transmitter and receiver is increased and the variation is studied.

3.1.2 Results

As suggested by the near-field effect where the received power diminishes with the cube of the radial distance, the received power is observed from Fig. 3.1B to fall rapidly within the first 0.5 m, as we venture into the far field however, the value of the received power diminished more slowly. It is also observed that there is a more constant near-field channel condition compared to the far-field and this can be seen in the low standard deviation. The near-field therefore shows a more reliable received power guarantee and the far field shows a higher variation in received values as the horizontal distance increases beyond 1.5 m. There is a high correlation between the 3 channel conditions around the 0.5 m mark. Overall, the received signal is highest in the Air2Air since this is homogeneous. There is no reciprocity in inhomogeneous communication as there is generally a better performance in the Air2Soil channel compared to the Soil2Air channel. With a loss of 100 dB experienced observed, which suggests a received power of -20 dBm, the feasibility of NFC in this inhomogeneous application is confirmed experimentally.

3.2 Tri-axis Coil Array

The proposed approach to this problem is to design a tri-axis coil array whose magnetic field can be aligned in any direction in a three-dimensional (3D) space based on the value of the current that is fed into the individual coils. The current can be varied to produce a constantly rotating magnetic field that would be varied in fixed steps with a period that is long enough to provide enough energy to any sensor in

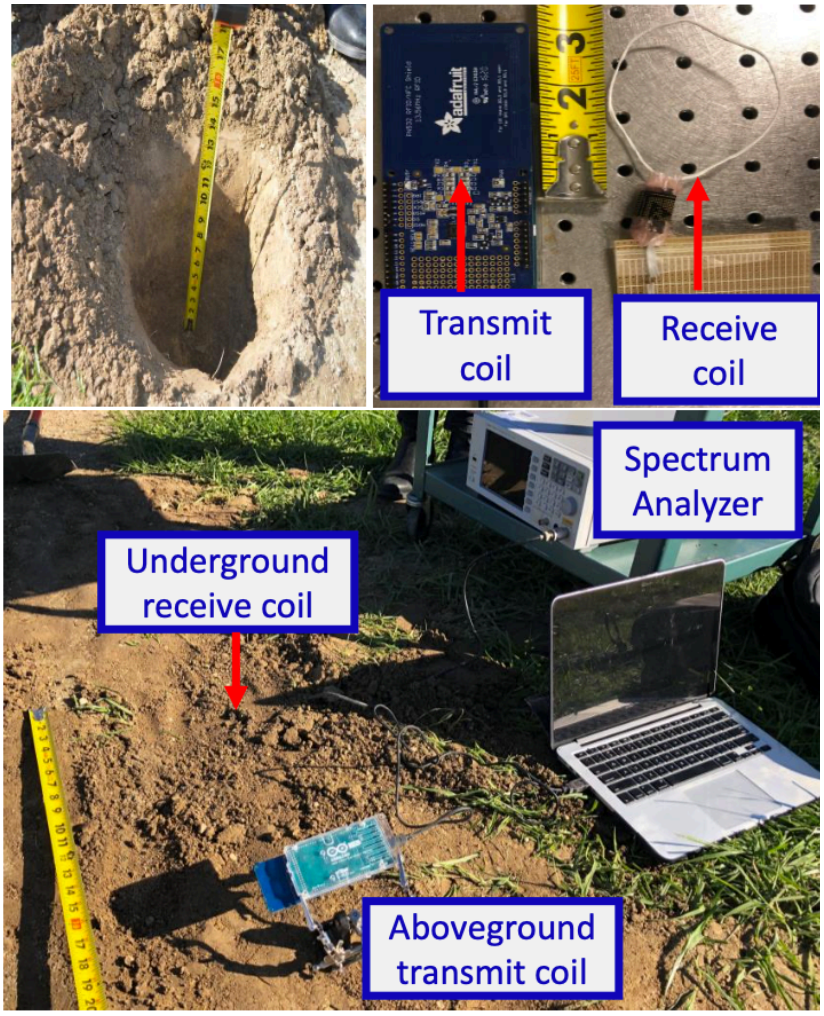

(A)

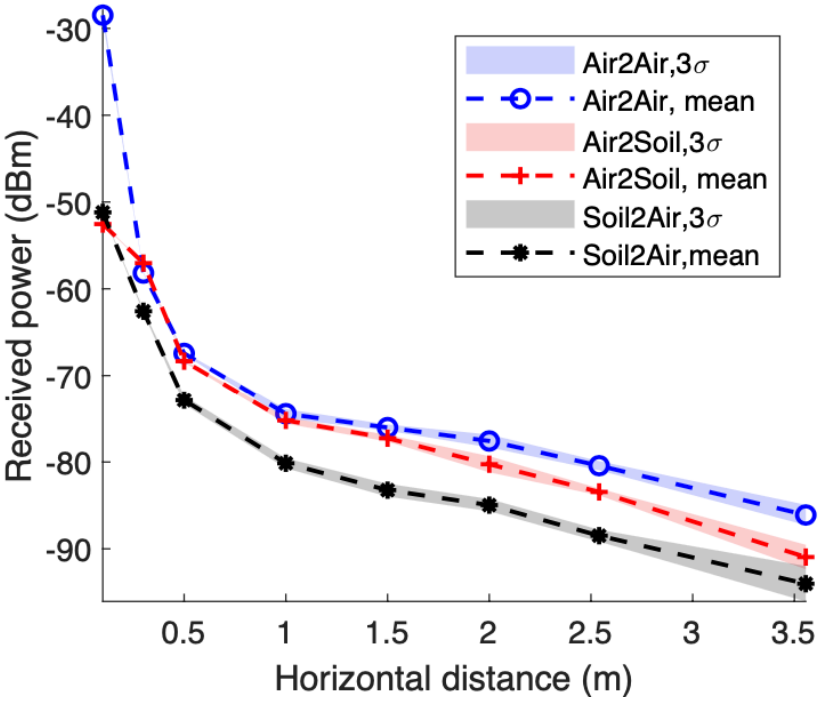

(B)

FIGURE 3.1: Fig. 3.1A shows the experimental equipment and setup used in data collection. Fig. 3.1B shows the variation of the received power with horizontal distance in each of the three channels defined.

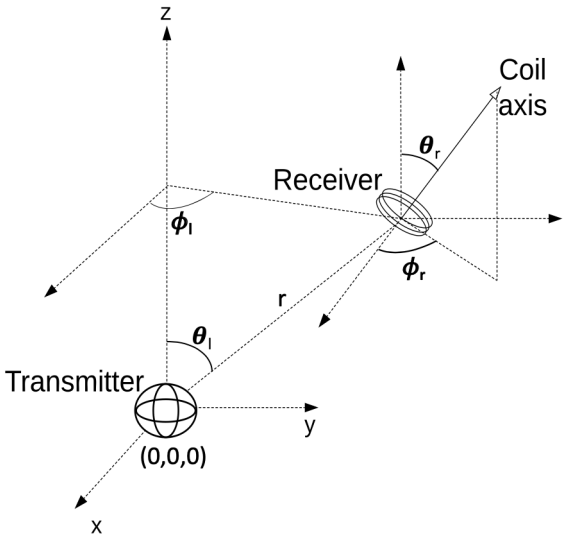

FIGURE 3.2: Illustration of the angular parameters used to describe the location(θ_l, ϕ_l) and orientation (θ_r, ϕ_r) of the receiver coil relative to the transmitter

a given direction to overcome its threshold voltage. The tri-axis coil, as shown in Fig. 3.2, has three coils with each coil axis aligned along each of the Cartesian plane axes (i.e., x, y, and z).

We define pseudo-axes for a unidirectional coil using a unit vector $\boldsymbol{n} = [x_n, y_n, z_n]^T$. Since the coil size is much smaller than the wavelength, we consider a coil as a magnetic dipole and the dipole moment has the same direction as $\boldsymbol{n}$. To facilitate our analysis, we consider the dipole moment is created by three magnetic dipoles which only generate x_n, y_n, and z_n, respectively. The tri-axis coil can be considered as an array of three magnetic dipoles that creates arbitrary x_n, y_n, and z_n by modulating the currents. Let the currents supplied to the coils with axes aligned along the x_n, y_n and z_n axis be i_1, i_2 and i_3. We assume the coils are identical and have the same radius $a_1 = a_2 = a_3 = a_t$ and number of turns $N_1 = N_2 = N_3 = N_t$. This simplifies the resultant formula for the magnetic field such that the total magnetic field observed at a point with spherical coordinates (r, θ_l, ϕ_l) relative to the transmitter can be represented in spherical coordinates as $\boldsymbol{h}_r = [h_{rr}, h_{r\theta}, h_{r\phi}]^T$.

Since the aim is to achieve direction control by changing the currents, we can use one variable $\boldsymbol{i} \in \mathbb{C}^3$ to denote coil currents, i.e., $\boldsymbol{i} = [i_1, i_2, i_3]^T$. Then, the beamforming problem simplifies to the problem of obtaining optimal $\boldsymbol{i}$. To achieve this

in a simplified manner, we introduce variables $C_r, C_\theta, C_\phi \in \mathbb{C}$ such that:

$$\boldsymbol{C} = \begin{bmatrix} C_r \\ C_\theta \\ C_\phi \end{bmatrix} = \begin{bmatrix} \frac{jka_t^2 N_t}{2r^2} \cdot [1 + \frac{1}{jkr}] \cdot e^{-jkr} \\ \frac{k^2 a_t^2 N_t}{4r} \cdot [1 + \frac{1}{jkr} - \frac{1}{(kr)^2}] \cdot e^{-jkr} \\ \frac{k^2 a_t^2 N_t}{4r} \cdot [1 + \frac{1}{jkr} - \frac{1}{(kr)^2}] \cdot e^{-jkr} \end{bmatrix} \tag{3.1}$$

where $j = \sqrt{-1}$, k is the propagation constant, a_t is the radius of the coil and r is the distance between the transmitter and the receiver. Then, the magnetic fields generated by a tri-axis coil derived in (Guo, Sun, and Wang, 2015b) can be represented in spherical coordinates as

$$\boldsymbol{h}_r = [h_{rr}, h_{r\theta}, h_{r\phi}]^T = \boldsymbol{C} \cdot \boldsymbol{\Gamma} \cdot \boldsymbol{i} \tag{3.2}$$

where

$$\boldsymbol{C} = \begin{bmatrix} C_r & 0 & 0 \\ 0 & C_\theta & 0 \\ 0 & 0 & C_\phi \end{bmatrix} \tag{3.3}$$

and

$$\boldsymbol{\Gamma} = \begin{bmatrix} \sin\theta_l \cos\phi_l & \sin\theta_l \sin\phi_l & \cos\theta_l \\ \cos\theta_l \cos\phi_l & \cos\theta_l \sin\phi_l & -\sin\theta_l \\ -\sin\phi_l & \cos\phi_l & 0 \end{bmatrix}, \tag{3.4}$$

where θ_l and ϕ_l are the angle parameters that are used to describe the location of the observation point, as shown in Fig. 3.2. Here, $\boldsymbol{C}$ is a function of distance, coil parameters, and environmental parameters and $\boldsymbol{\Gamma}$ is a function of the observation point location in the 3D space. For example, if receivers located on a sphere with the transmitter with a tri-axis coil in the center, they have the same $\boldsymbol{C}$ but different $\boldsymbol{\Gamma}$.

Magnetic field $\boldsymbol{h}_r$ is obtained in a Spherical Coordinates System (SCS), while the coil orientation is described in a Cartesian Coordinates System (CCS). By using the following equation, we can obtain $\boldsymbol{h}_r$ in a CCS,

$$\boldsymbol{h} = \boldsymbol{T} \cdot \boldsymbol{h}_r, \tag{3.5}$$

where

$$\boldsymbol{T} = \begin{bmatrix} \sin\theta_l \cos\phi_l & \cos\theta_l \cos\phi_l & -\sin\phi_l \\ \sin\theta_l \sin\phi_l & \cos\theta_l \sin\phi_l & \cos\phi_l \\ \cos\theta_l & -\sin\theta_l & 0 \end{bmatrix}. \tag{3.6}$$

The aim is to produce an optimal magnetic field in the intended direction of observation and aligning the magnetic field vector in the direction of a unit vector along the axis of a coil at the observation point would be greatly desired. We define this unit vector as $\boldsymbol{u} \in \mathbb{R}^3$ such that:

$$\boldsymbol{u} = [\sin\theta_r \cos\phi_r, \sin\theta_r \sin\phi_r, \cos\theta_r]^T, \tag{3.7}$$

where θ_r and ϕ_r describe the orientation of the receiver coil axis, as shown in Fig. 3.2. To find three optimal current values can be complex in nature. This problem, can be modeled as an optimization problem that aims to reduce the distance between the resultant magnetic field and the unit vector in the direction of orientation of a coil at the observation point. We define a power threshold P_{max} which should not be exceeded in supplying power to the antenna coils. We define a diagonal matrix $\boldsymbol{R} \in \mathbb{R}^{3\times3}$ representing the resistances of the tri-axis coil where r_x is the resistance of transmitter coil x and $r_1 = r_2 = r_3 = r_t$ such that:

$$\boldsymbol{R} = \begin{bmatrix} r_t & 0 & 0 \\ 0 & r_t & 0 \\ 0 & 0 & r_t \end{bmatrix}, \tag{3.8}$$

where r_t is the transmitter coil resistance. The resultant magnetic field $\boldsymbol{h}$ should also induce a voltage large enough to overcome the threshold voltage in the receiver power harvesting circuit. The induced voltage v can be expressed as:

$$v = -\omega \mu_r \mu_0 N_r \pi a_r^2 \boldsymbol{h} \cdot \boldsymbol{u}, \tag{3.9}$$

where μ_r is the relative permeability of the medium and μ_0 is the permeability of free space, N_r is the number of turns of the receiver coil and a_r is the radius of the receiver coil.

3.3 Model Design

To efficiently charge batteryless sensors, we need to maximize the induced voltage given limited transmission power. If we have the knowledge of the receiver's coil orientation $\boldsymbol{u}$, this problem can be efficiently solved. However, in this paper, we assume we have no knowledge of $\boldsymbol{u}$, thereby it is impossible to obtain the optimal $\boldsymbol{i}$.

To overcome the threshold voltage and efficiently charge coils with arbitrary orientations, we use MagBB and an example is shown in Fig. 3.3. First, when we use constant currents for tri-axis coils, the generated magnetic field always points to one direction. Different from electromagnetic wave-based wireless communication/charging in the terrestrial environments, the magnetic induction-based wireless communication/charging operates in the near field with a short distance, where the multipath fading can be neglected. As shown in the upper of Fig. 3.3a, if the magnetic field direction is parallel with the receiver's coil axis, the received power can be maximized. However, if the magnetic field direction is perpendicular to the receiver's coil axis, no voltage can be induced. Thus, the performance of using constant currents for the tri-axis coil is highly random, which is not predictable nor reliable without the knowledge of $\boldsymbol{u}$.

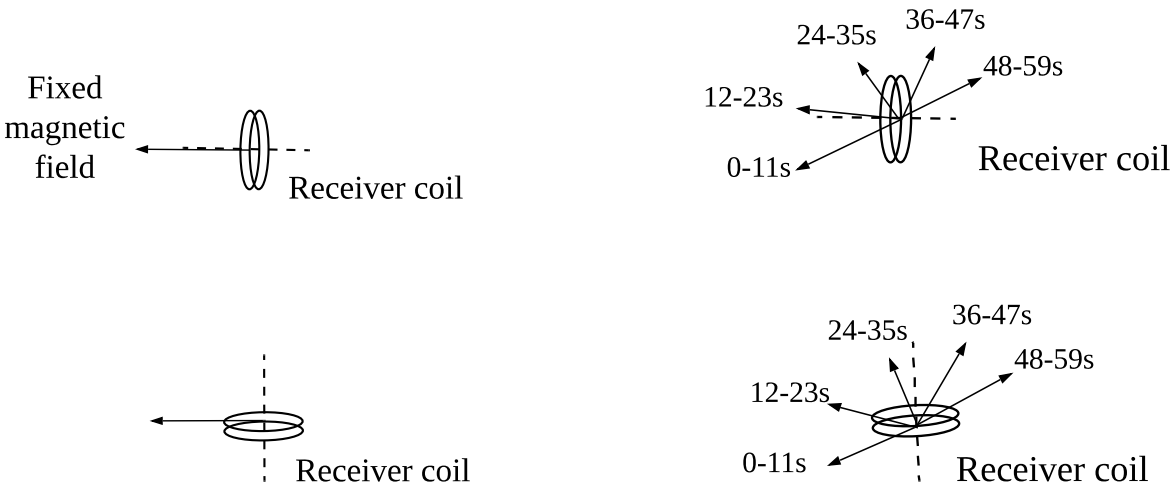

(A) Constant transmitter current supply to charge randomly oriented coils

(B) Transmitter current set rotating magnetic field through space.

FIGURE 3.3: Illustration comparing performance of constant and rotating magnetic fields for different receiver coil orientations. Fig. 3.3A shows two instances where maximum voltage is induced when coil axis is aligned with magnetic field (top) and zero voltage induced when coil axis is perpendicular to magnetic field (bottom). Fig. 3.3B shows how voltage is induced in the receiver coil by the rotating magnetic field at some points during the charging cycle irrespective of coil orientation.

MagBB is based on current vector rotation. As shown in Fig. 3.3b, 5 current vectors are used to create 5 magnetic fields with different directions (their magnitudes may also be different). For example, if we use 60 seconds to charge a sensor, each current vector is allocated with 12 seconds. Since the 5 vectors cover 180 degrees, we can ensure that coils with arbitrary orientations can be covered and at least one current vector can induce voltage that is larger than the threshold voltage to charge a sensor. Next, we try to study the following three problems: 1) how to design the current vectors? 2) how many current vectors do we need? and 3) does the current vector depend on the receiver's location?

Current Vector Design

Assume we have the knowledge of the receiver's location. Then, we create n_{cv} current vectors to rotate the magnetic field direction for 180 degrees. The following

problem is formulated to obtain the current vector $\boldsymbol{i}$,

$$\text{(P1): } \underset{\boldsymbol{i}\in\mathbb{C}^3}{\text{minimize}} \left\| \boldsymbol{u} - \frac{\boldsymbol{h}}{\| \boldsymbol{h} \|} \right\|^2 \tag{3.10}$$

$$s.t.\ \boldsymbol{i}^T \boldsymbol{R} \boldsymbol{i} \leq 2P_{max}; \tag{3.11}$$

$$|\boldsymbol{h}^T \boldsymbol{u}| > \frac{v_{th}}{\omega \mu_r \mu_0 N_r \pi a_r^2}, \tag{3.12}$$

where $\boldsymbol{u}$ is the targeting magnetic field direction. The objective function aims to design the magnetic field to point to the desired direction. The first constraint is due to the transmission power and the second constraint ensures the induced voltage is larger than the rectifier's threshold voltage v_{th}. Consider the targeting magnetic field directions as $\{\boldsymbol{u}_l, l = 1, \cdots, n_{cv}\}$. By substituting $\{\boldsymbol{u}_l, l = 1, \cdots, n_{cv}\}$ into the above problem, we can obtain the associated current vectors.

However, directly solving (P1) is challenging. In order to homogenize this optimization problem, a slack variable $t \in \mathbb{R}$ is introduced such that:

$$t = \| \boldsymbol{h} \| \text{ and } t^2 = \boldsymbol{i}^H \cdot \hat{\boldsymbol{C}}^H \cdot \hat{\boldsymbol{C}} \cdot \boldsymbol{i}. \tag{3.13}$$

where $\hat{\boldsymbol{C}} = \boldsymbol{C}\boldsymbol{\Gamma}$ The objective function can then be rewritten as

$$\text{(P2): } \underset{\boldsymbol{i}\in\mathbb{C}^3}{\text{minimize}} \| t\boldsymbol{u} - \boldsymbol{h} \|^2 \tag{3.14}$$

$$s.t.\ \boldsymbol{i}^H \hat{\boldsymbol{C}}^H \hat{\boldsymbol{C}} \boldsymbol{i} = t^2 \tag{3.15}$$

$$\boldsymbol{i}^H \boldsymbol{R} i \leq 2P_{max} \tag{3.16}$$

$$\boldsymbol{i}^H \hat{\boldsymbol{C}}^H \boldsymbol{u}\boldsymbol{u}^T \hat{\boldsymbol{C}} \boldsymbol{i} > \frac{V_{th}^2}{\omega^2 (\mu_r \mu_0 N_r \pi a_r^2)^2} \tag{3.17}$$

which can subsequently be solved using the method of Semidefinite Relaxation (Luo et al., 2010).

Our ability to use Semidefinite Relaxation is incumbent on the ability to express our problem in the form $\boldsymbol{x}^T \boldsymbol{A} \boldsymbol{x}$ where $\boldsymbol{x} \in \mathbb{C}^N$ is the variable or system of variables to be optimized and $\boldsymbol{A} \in \mathbb{C}^{N\times N}$ is a function or group of functions with known

values that constitute a positive semidefinite matrix. Since the value of $\boldsymbol{i}$ could be complex in nature, the optimization problem can be expressed as a real value equation whereby we decompose all potentially complex values into their real and imaginary forms such that:

$$\bar{\boldsymbol{u}} = \begin{bmatrix} \Re\{\boldsymbol{u}\} \\ \Im\{\boldsymbol{u}\} \end{bmatrix}, \quad \bar{\boldsymbol{i}} = \begin{bmatrix} \Re\{\boldsymbol{i}\} \\ \Im\{\boldsymbol{i}\} \end{bmatrix}, \tag{3.18}$$

$$\bar{\boldsymbol{C}} = \begin{bmatrix} \Re\{\hat{\boldsymbol{C}}\} & -\Im\{\hat{\boldsymbol{C}}\} \\ \Im\{\hat{\boldsymbol{C}}\} & \Re\{\hat{\boldsymbol{C}}\} \end{bmatrix} \tag{3.19}$$

$$\bar{\boldsymbol{R}} = \begin{bmatrix} \Re\{\boldsymbol{R}\} & -\Im\{\boldsymbol{R}\} \\ \Im\{\boldsymbol{R}\} & \Re\{\boldsymbol{R}\} \end{bmatrix}. \tag{3.20}$$

This decomposition essentially doubles all dimensions such that all any matrix $\boldsymbol{X} \in \mathbb{C}^{N\times N}$ becomes $\boldsymbol{X} \in \mathbb{R}^{2N\times 2N}$ and all vectors $\boldsymbol{x} \in \mathbb{C}^N$ become $\boldsymbol{x} \in \mathbb{R}^{2N}$, i.e., $\boldsymbol{u}$ and $\boldsymbol{i}$ become 6×1 matrices and $\hat{\boldsymbol{C}}$ becomes a 6×6 matrix. The homogenized objective function $\| t\boldsymbol{u} - \boldsymbol{h} \|^2$ can then be accurately written as:

$$\begin{bmatrix} \bar{\boldsymbol{i}}^T & t \end{bmatrix} \boldsymbol{A} \begin{bmatrix} \bar{\boldsymbol{i}} \\ t \end{bmatrix} = \begin{bmatrix} \bar{\boldsymbol{i}}^T & t \end{bmatrix} \begin{bmatrix} \bar{\boldsymbol{C}}^T\bar{\boldsymbol{C}} & -\bar{\boldsymbol{C}}^T\bar{\boldsymbol{u}} \\ -\bar{\boldsymbol{u}}^T\bar{\boldsymbol{C}} & \| \bar{\boldsymbol{u}} \|^2 \end{bmatrix} \begin{bmatrix} \bar{\boldsymbol{i}} \\ t \end{bmatrix}. \tag{3.21}$$

In this form, we can adequately apply semidefinite programming in solving this problem. We can express a single variable $\boldsymbol{\beta} \in \mathbb{R}^{7\times 7}$ as the product of our variable matrix and its transpose:

$$\begin{bmatrix} \bar{\boldsymbol{i}} \\ t \end{bmatrix} \begin{bmatrix} \bar{\boldsymbol{i}}^T & t \end{bmatrix} = \boldsymbol{\beta}. \tag{3.22}$$

The algorithm to be employed based on the objective function and constraints is given in Algorithm 1.

Algorithm 1: Code for optimization problem (P2)

1: Variable $\boldsymbol{\beta}$ symmetric
2: minimize$(trace(\boldsymbol{A} * \boldsymbol{\beta}))$
3: subject to
4: $\quad trace(\bar{\boldsymbol{R}} \cdot \boldsymbol{\beta}(1{:}6,1{:}6)) \leq 2P_{max}$
5: $\quad trace(\bar{\boldsymbol{C}}^T \bar{\boldsymbol{C}} \cdot \boldsymbol{\beta}(1{:}6,1{:}6)) = \boldsymbol{\beta}(7,7)$
6: $\quad trace((\bar{\boldsymbol{C}}^T \boldsymbol{u}\boldsymbol{u}^T \bar{\boldsymbol{C}}) \cdot \boldsymbol{\beta}(1{:}6,1{:}6)) \geq \frac{V_{th}^2}{\omega^2(\mu_r \mu_0 N \pi a^2)^2}$

The approximated solution is a rank-1 matrix $\boldsymbol{\beta}$ and to obtain the approximated $\boldsymbol{i}$ we use the dominant eigenvector:

$$\boldsymbol{\beta} \approx \lambda_{max} \boldsymbol{q}\boldsymbol{q}^T, \tag{3.23}$$

where $\lambda_{max} \in \mathbb{R}$ is the largest eigenvalue of matrix $\boldsymbol{\beta} \in \mathbb{R}$ and $\boldsymbol{q} \in \mathbb{R}^{N\times 1}$ is the eigenvector associated with λ_{max}. The eigenvector that is associated with the largest eigenvalue of $\boldsymbol{\beta}$ is considered as the solution $\boldsymbol{i}$. From this approximation, the optimal decomposed current vector can be obtained as $\boldsymbol{i}^\star \in \mathbb{R}^{7\times 1}$ such that:

$$\boldsymbol{i}^\star = \sqrt{\lambda_{max}} \cdot \boldsymbol{q}, \tag{3.24}$$

with

$$\begin{bmatrix} \Re\{\boldsymbol{i}_1\} \\ \Re\{\boldsymbol{i}_2\} \\ \Re\{\boldsymbol{i}_3\} \end{bmatrix} = \boldsymbol{i}^\star(1:3); \quad \begin{bmatrix} \Im\{\boldsymbol{i}_1\} \\ \Im\{\boldsymbol{i}_2\} \\ \Im\{\boldsymbol{i}_3\} \end{bmatrix} = \boldsymbol{i}^\star(4:6). \tag{3.25}$$

The performance of a given set of currents is then obtained by finding the optimum current for a coil in a given location and in all possible directions of orientation. The efficacy of this system lies in its ability to induce a voltage in a randomly oriented coil at a given location for a sufficiently long period such that the induced voltage $v > v_{th}$.

Number of Current Vectors

We cycle through the current set in a fast enough manner in order to keep the sensors charged. For a given set of current values, therefore, we charge the sensor long enough such that all the currents in the current set are applied for an equal time interval of ΔT, i.e., where T_c is the overall charging time. Here, there is a trade-off between the charging efficiency and the charging time interval of ΔT. On one hand, if n_{cv} is large, with high probability, we can obtain the optimal (or nearly optimal) current vector to charge the receiver with near-zero orientation loss. On the other hand, a large n_{cv} reduces ΔT since the T_c is a constant. Even if the charging efficiency is high, a small ΔT may reduce the overall received energy. Since the receiver's orientation $\boldsymbol{u}$ is an arbitrary vector in 3D space, to fully capture all possibilities, we need three current vectors at least. Otherwise, if $n_{cv} < 3$, there are some blind points. On the contrary, there is no limitation on the maximum number of current vectors since with more current vectors, we can cover more orientations. However, as the number increases, the complexity of the algorithms increases, and the correlation between two adjacent current vector increases, which may waste resources.

The minimum number of current vectors, i.e., 3 mutually orthogonal receiver coil orientations, can be designed in the following way. We define three random vectors $\boldsymbol{v_1}, \boldsymbol{v_2}, \boldsymbol{v_3} \in \mathbb{R}^{3\times 1}$ based on which we derive orthogonal basis $\boldsymbol{u_1}, \boldsymbol{u_2}, \boldsymbol{u_3} \in \mathbb{R}^{3\times 1}$ using Gram–Schmidt process such that:

$$\boldsymbol{u_1} = \boldsymbol{v_1} \tag{3.26}$$

$$\boldsymbol{u_2} = \boldsymbol{v_2} - \frac{\boldsymbol{v_2} \cdot \boldsymbol{u_1}}{\|\boldsymbol{u_1}\|^2}\boldsymbol{u_1} \tag{3.27}$$

$$\boldsymbol{u_3} = \boldsymbol{v_3} - \frac{\boldsymbol{v_3} \cdot \boldsymbol{u_1}}{\|\boldsymbol{u_1}\|^2}\boldsymbol{u_1} - \frac{\boldsymbol{v_3} \cdot \boldsymbol{u_2}}{\|\boldsymbol{u_2}\|^2}\boldsymbol{u_2} \tag{3.28}$$

By normalizing $\boldsymbol{u_1}$, $\boldsymbol{u}_2$, and $\boldsymbol{u}_3$, we obtain the orthonormal basis $\boldsymbol{e_1, e_2, e_3} \in \mathbb{R}^{3\times 1}$ which represent three mutually orthogonal coil directions such that:

$$e_n = \frac{\boldsymbol{u_n}}{\|\boldsymbol{u_n}\|} \tag{3.29}$$

Knowledge of these orientations can then be used in finding the optimum currents for a coil aligned along these directions by substituting into (3.10).

Receiver Location Dependency

Note that, we optimize the current vectors at one specific location. Next, we explore how the location of a receiver coil affects the magnetic field intensity, and how to maximize this field. From (3.2), we introduce the scalar and angular coefficients of the equation. It can be seen that $\boldsymbol{\Gamma}$ is an orthogonal matrix since $\boldsymbol{\Gamma\Gamma}^T = \boldsymbol{\Gamma}^T\boldsymbol{\Gamma} = \boldsymbol{I}$. The angular coefficient, therefore, does not affect the magnitude of the generated magnetic field vector but would only either reflect it in some plane or rotate it. The factor affecting the efficacy of a given current vector set in any location would, therefore, depend principally on the scalar coefficient $\boldsymbol{C}$. From (3.1), it can be seen that $C_\theta = C_\phi$. Also, it can be seen, quite intuitively, that the scalar coefficient magnitudes are inversely proportional to r. In the near field of the coil antenna ($r \ll \text{wavelength}/2\pi$),

$$C_r \approx 2C_\theta \approx 2C_\phi. \tag{3.30}$$

The induced voltage is proportional to $\boldsymbol{h}_r$ which is given in (3.2). Since $\boldsymbol{\Gamma}$ is an orthogonal matrix, $\boldsymbol{h}_r$ is equivalent to the result of projecting $\boldsymbol{i}$ in a new orthogonal coordinates system using $\boldsymbol{\Gamma}$ and then scaled by the three elements using C_r, C_θ, and C_ϕ. Given the distance, C_r, C_θ, and C_ϕ do not change on the sphere. In the near field, due to (3.30), $\boldsymbol{h}_r$ are similar, which does not depend on the location on the sphere. Assuming the applied current is at its maximum accepted value such that $\|\boldsymbol{i}\|^2_{\max} = \frac{2P_{\max}}{r_t}$, then $C_\theta\|\boldsymbol{i}\|_{\max} \leq \|\boldsymbol{h}\| \leq C_r\|\boldsymbol{i}\|_{\max}$ and this stands true for the near-field region. This relatively low variation in magnetic field intensity as the receiver

location changes for a constant current is very convenient for reliable charging of a receiving sensor.

However, as we venture into the far field ($kr >> 1$)(Balanis, 2016), the scalar coefficient values start to diminish such that $C_r << C_\theta \approx C_\phi$. In this case, the projected $\boldsymbol{i}$ is scaled unevenly. If the projected vector has a dominant element and it is scaled by C_r, the $\boldsymbol{h}_r$ can be extremely small. The magnitude of the magnetic field can, therefore, vary widely as the receiver location changes, potentially resulting in erratic charging efficiency as the produced voltage can drop below the desired value with a slight change in the relative location of the receiver to the transmitter. This makes a far field application of this implementation relatively suboptimal.

4 NUMERICAL SIMULATION AND RESULTS

In this section, various simulations are carried out to numerically analyze, compare, and contrast the performance of the blind beamforming scheme under various conditions. We first evaluate the induced voltage and then we generate randomly oriented receiving coils and compare the reliability of different approaches. The employed values for the simulations are shown in Table 4.1.

4.1 Magnetic Field Vector Distribution

Initial results of this simulation have been documented in (Ofori and Guo, 2021) which was presented at the 18th Annual Consumer Communications Networking Conference (CCNC). These results however made use of a more simplistic methodology in selecting the optimization locations which did not ensure an equal distribution within a 3-dimensional (3D) space. We introduce an additional constraint that seeks to improve the spatial distribution of optimized vector locations. In order to ensure that the magnetic field covers as much of a 3D space as possible, the locations chosen, based on which optimized currents are calculated, should be evenly spread out in space. The number of current values that are chosen for optimization should then be distributed as uniformly as possible. To ensure this, two conditions need to be satisfied in finding the optimal θ and ϕ values that characterize the location of a receiver coil; the number of locations M_i along the circular plane at a given θ_i is such that $M_i \propto \sin\theta_i$. Secondly, as shown in Fig. 4.1, for 3 adjacent locations in a 3D space, along the polar and azimuthal planes, the difference between distances, d_1 and d_2 should be minimized. We therefore find the number of θ values N at which $\|d_1 - d_2\|$ is minimum. We can express $\|d_1 - d_2\|$ as a function of N and find the argmin of this function. We note that the θ values should be equally

TABLE 4.1: Simulation Parameters

Symbol	Value	Symbol	Value
μ_r	1	f	13.56 MHz
ϵ_o	8.85×10^{-12} F/m	ϵ_r	1.0006
a_t	0.1 m	a_r	0.01 m
$P_{\max}$	50 W	v_{th}	0.2 V
r_t	1 Ω	r_r	0.2 Ω

spaced between 0 and $\frac{\pi}{2}$ and the ϕ values along a given circular plane at θ_i should be equally distributed from 0 to 2π. In this formulation, we note that θ_1 is always 0, and M_1 (The number of ϕ locations at θ_1) is always equal to 1 since the location of a receiver at $\theta = 0$ will always be the same no matter the value of ϕ. We can therefore express M_i such that:

$$M_i = \begin{cases} 1, & \text{if } i = 1 \\ \lfloor \frac{(n_{cv}-1)\sin\theta_i}{\sum_{j=2}^{N}\sin\theta_j} \rceil, & \text{otherwise} \end{cases} \tag{4.1}$$

where i > 0, n_{cv} is the number of current vectors which we seek to distribute, and $\lfloor k \rceil$ is the value of k rounded to the nearest integer. We then obtain three adjacent points in spherical coordinates in the form $P(r, \theta, \phi)$ such that $P_1(1, \theta_k - \frac{\pi}{N-1}, 0)$, $P_2(1, \theta_k, 0)$ and $P_3(1, \theta_k, \frac{2\pi}{M_k-1})$, where θ_k is the first polar angle at which $M_k > 0$. $\|d_1 - d_2\|$ can then be expressed as:

$$\|d_1 - d_2\| = \|d(P_1, P_2) - d(P_2, P_3)\| \tag{4.2}$$

where $d(\cdot, \cdot)$ is the euclidean distance between two locations. This process has been detailed in Algorithm 2.

4.2 Comparison of Induced Voltage

The performance of this system using a current set optimized for randomly oriented coil at a predetermined location 1.0 m directly below the transmitter ($\theta_l = 180°$,

Algorithm 2: Uniform Distribution Algorithm

Input: N
Output: $diff$
Function `FindEuclideanDiff(`N`)`**:**
  $\theta_1 \longleftarrow 0$;
  $M_1 \longleftarrow 1$;
  $sineTotal \longleftarrow \sum_{j=2}^{N} \sin\left(\frac{(j-1)\pi}{N-1}\right)$;
  for $i \longleftarrow 2$ *to* N **do**
    $M \longleftarrow \left\lfloor \frac{(n_{cv}-1)\sin\left(\frac{(i-1)\pi}{N-1}\right)}{sineTotal} \right\rceil$;
    if $M \geq 2$ **then**
      $t \longleftarrow i$;
      break;
    end
  end
  $P_1(1, \frac{(t-2)\pi}{N-1}, 0)$;
  $P_2(1, \frac{(t-1)\pi}{N-1}, 0)$;
  $P_3(1, \frac{(t-1)\pi}{N-1}, \frac{2\pi}{M-1})$;
  $diff \longleftarrow \|d(P_1, P_2) - d(P_2, P_3)\|$
  return $diff$
End Function
Procedure `MinimizeEuclideanDiff(`N`)`**:**
  return $\lfloor \underset{N}{\operatorname{argmin}}$ `FindEuclideanDiff(`N`)` $\rfloor$
End Procedure

TABLE 4.2: LOCATION PARAMETERS

Simulation Locations	θ_l	ϕ_l
Optimized location	180°	0°
Random location	99.1°	254.9°

$\phi_l = 0°$), which is called the "Optimized location" in figures 4.2, 4.3 and 4.8. This performance is compared with that of a random location given in Table 4.2, which is called "Random Location", in figures 4.2, 4.3 and 4.8. To do this, the various coil orientations are cycled through uniformly distributed points in a 3-dimensional spherical region. Figures 4.2, 4.3 and 4.8 show the voltage induced within a one-minute charging cycle. Figures 4.4, 4.5, 4.6 4.7 and 4.9 compare the performance based on the total energy induced for various radial distances, locations, and orientations as outlined in the following sections.

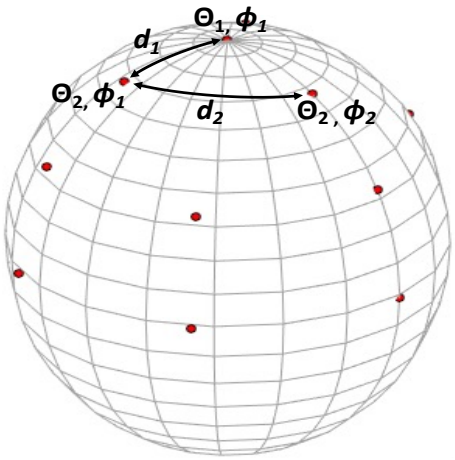

FIGURE 4.1: Illustration showing uniformly distributed points of optimization

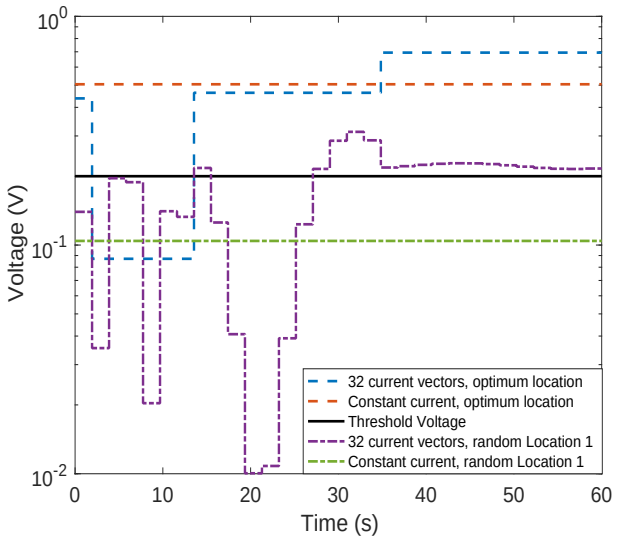

FIGURE 4.2: Induced voltage in the receiver coil using 32 blind beamforming current vectors at the optimized location and a randomly selected location.

The performance of the system as the number of currents increases is studied between two optimized current sets; one set of currents for 16 combinations of θ_r and ϕ_r throughout a hemispherical range and another for 32 currents giving a better resolution. The corresponding current values are calculated based on the optimization method outlined in Algorithm 1. The voltages induced at the indicated locations are then compared to find out how the MagBB algorithm performs in optimum locations relative to unknown locations, which will be the case for the intended application. Lastly, a simplistic approach is employed by finding the maximum balanced current without exceeding the maximum allowable current to the transmitter coils

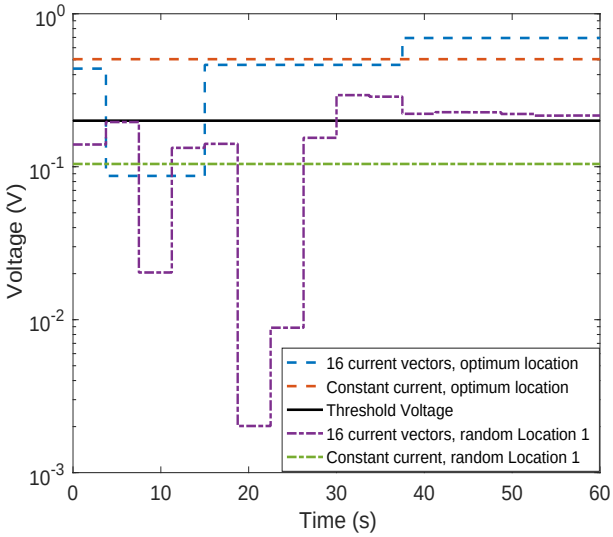

FIGURE 4.3: Induced voltage in the receiver coil using 16 blind beamforming current vectors at the optimized location and a randomly selected location.

per the power requirements specified for this system. i.e.,

$$\boldsymbol{i} = \sqrt{\frac{2P_{\max}}{3r_t}}[1,1,1]^T \tag{4.3}$$

The induced voltage is calculated and compared to MagBB for the same locations under simulation. Since the circuitry can be configured to invert negative voltages, the working range of the sensor consists of all induced voltages v such that $|v| > v_{th}$.

Fig. 4.3 and Fig. 4.2 show this comparison for the 16-current and 32-current sets respectively. In both cases, the optimized current vectors show a clear advantage here as it is able to charge coils at both receiver locations above the threshold voltage at certain points within the charging cycle. The constant current, however, either works throughout the charging cycle (optimized location) or does not charge the receiver at all throughout the charging cycle (random location). This, therefore, makes the simplistic approach sub-optimal for simultaneous charging at multiple locations. Comparing the two optimized current vectors, the 32-current set

appears to charge the receiver more continuously given the higher resolution afforded by more current sets and more continuous rotation in the three-dimensional space. This resolution also enables the alignment of the magnetic field at certain positions that may adequately charge the coil while the 16-current set may miss such locations. For instance, between 15 and 18s seconds, the 32-current set in Fig. 4.2 charges a coil at the random location midway during this period. However, the voltage induced by the 16-current set during the same period remains below the threshold. However, the upsides observed in this manner are few and may not justify the additional computational burden to achieve a higher resolution.

We explore the necessity and possibility of reducing this computational burden by producing a set of current vectors optimized for three mutually orthogonal coil orientations which are then tested in comparison with the constant current sets for the same locations as shown in Table 4.2. These currents are calculated by determining the orthonormal bases of 3 randomly generated unit vectors representing three magnetic field alignments. The optimum current values are then found for each vector using the Algorithm 1. The performance is observed as shown in Fig. 4.8 and Fig. 4.9. These current vectors can also achieve high induced voltage. Also, this method provides more directional diversity compared with the constant current.

4.3 Reliability Evaluation

The energy performance of the various current sets for fixed locations at 0.5 m and at 1.0 m is then analyzed for 32, 16, 8 and 3 current vectors to find out the dependence the system performance on the number of current vectors. The general performance is appraised by finding the total energy delivered to 10,000 randomly positioned receivers assuming the receivers are only charged by voltages above the threshold voltage. The receiving coils are randomly orientated by letting their axes point to a random point on a unit sphere. Then, we calculate the received energy during one charging cycle. To make a fair comparison, one cycle is considered to be

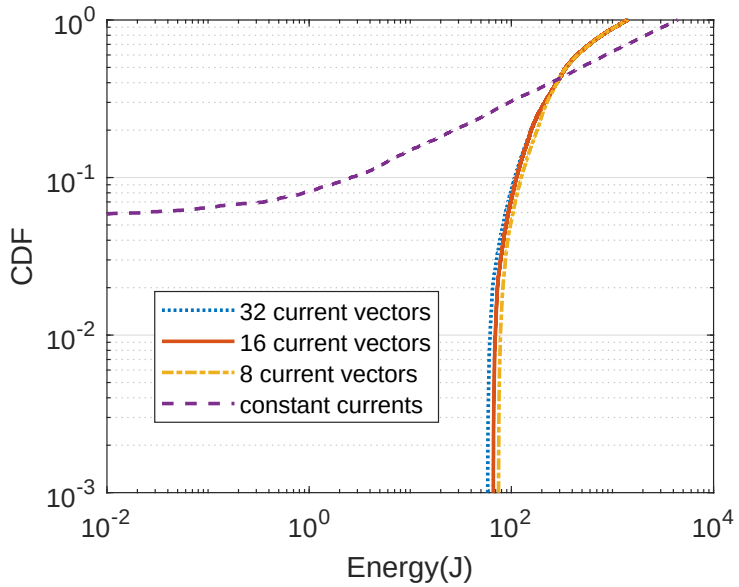

FIGURE 4.4: CDF using 8, 16, and 32 blind beamforming current vectors at a fixed location ($\theta_l = 180°$,$\phi_l = 0°$) with a distance of 0.5 m

60 s, and a single current vector within the set uses $60/n_{cv}$ s. Then, the CDFs (Cumulative Distribution Function) for various policies are plotted to compare their performances.

First, in Fig. 4.5 and 4.4, the receiver location is fixed and randomly generated orientation is used. The results show that when the distance is 1.0 m using a constant current vector, around 40% of the receivers cannot be charged at all. If we use MagBB, the percentage decreases to nearly zero as the number of current vectors increases. For a shorter distance of 0.5 m, we have the same observation but the percentage is much lower. Also, it is observed bwtween corresponding number of current vectors between Fig. 4.5 and 4.4 that the received energy decreases dramatically as the distance increases. This is due to the small size of the receiving coil. Since the batteryless sensors have low power consumption, the harvested energy at the level of 1 mJ can be sufficient. Also, the charging time can be increased to meet the requirement of high-power-consumption sensors.

In Fig. 4.6 and 4.7, both the receiver location and coil orientation are varied. The comparison here suggests that there is a 35% probability that a randomly oriented coil is not charged at all by a constant current compared to about 2% for 8 current

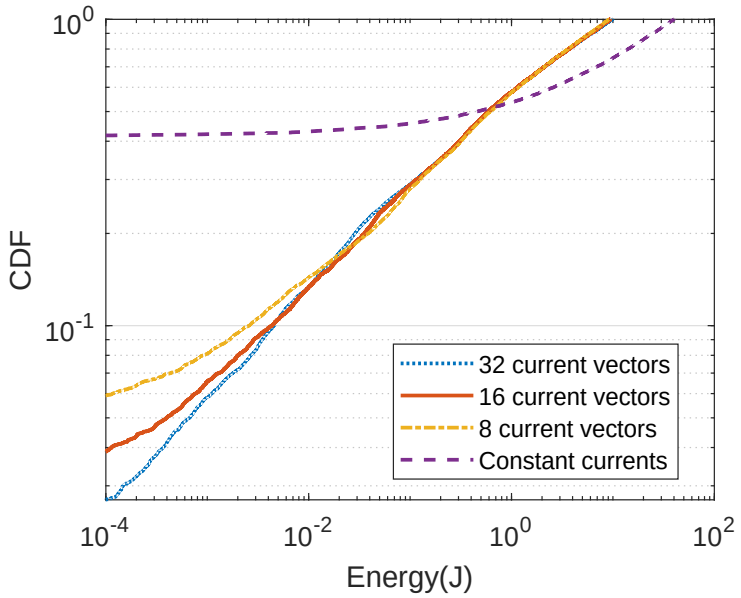

FIGURE 4.5: CDF using 8, 16, and 32 blind beamforming current vectors at a fixed location ($\theta_l = 180°$,$\phi_l = 0°$) with a distance of 1.0 m

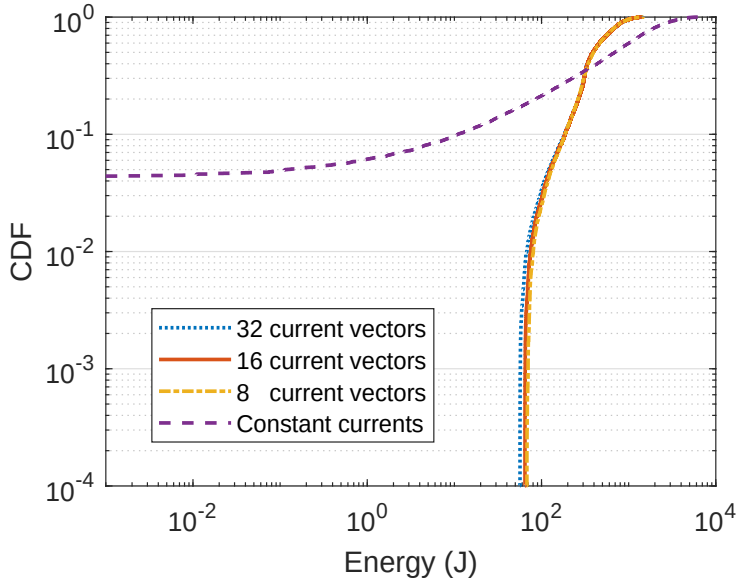

FIGURE 4.6: CDF comparing energy induced at random coil locations and orientations by different current sets at a distance of 0.5 m

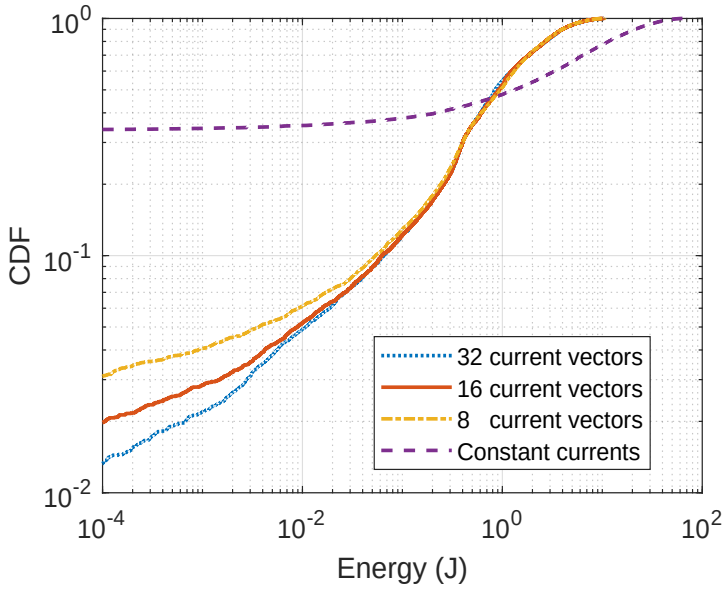

FIGURE 4.7: CDF comparing energy induced at random coil locations and orientations by different current sets at a distance of 1 m

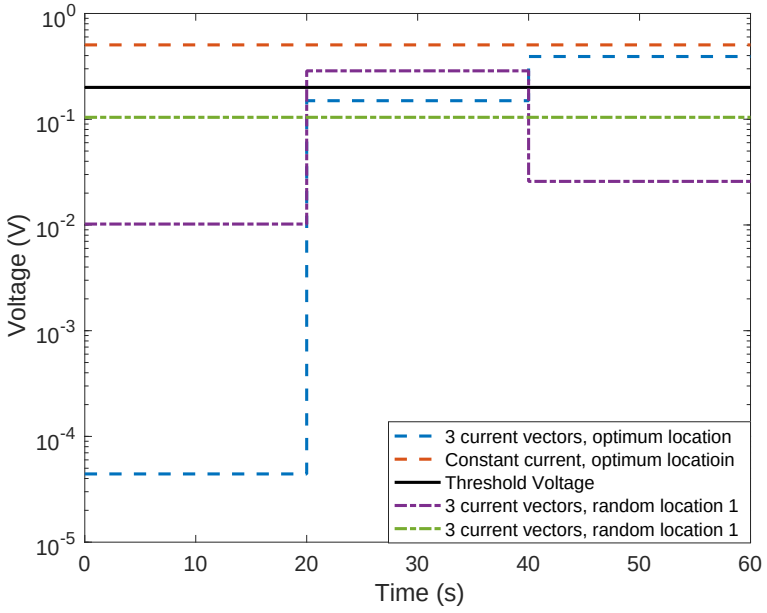

FIGURE 4.8: Induced voltage in the receiver coil using 3 orthogonal blind beamforming current vectors. Location 1 is the optimized position and location 2 is a randomly selected location.

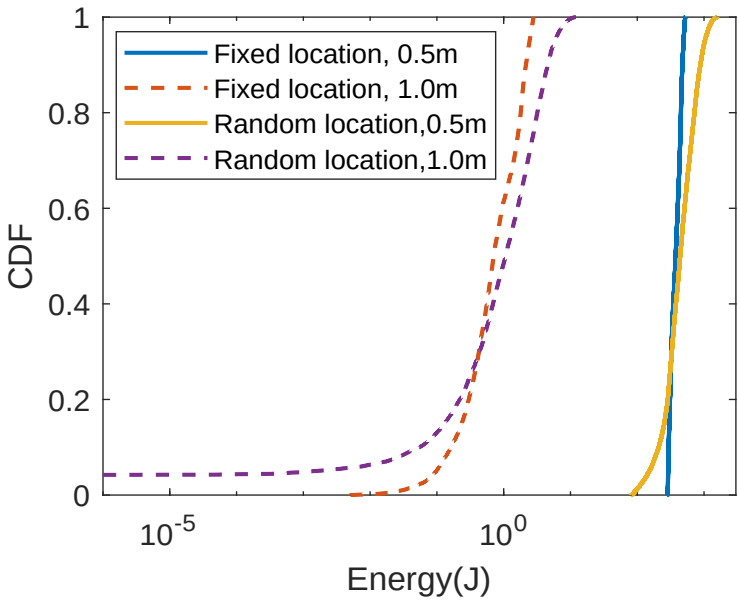

FIGURE 4.9: CDF showing the performance of current set optimized for 3 mutually orthogonal receiver orientations at 0.5 m and 1.0 m radial distance

vectors and <1% for 16-current and 32-current sets at 1.0 m. The performance gains achieved by using the optimized current sets are more pronounced at 1.0 m than at 0.5 m. An 8-current set is therefore more computationally light and produces similar performance at 0.5 m to the more computationally heavy 16 and 32-current sets. Noticeable differences in performance are seen beyond 1 m.

To evaluate the performance of the minimum number of current vectors, i.e., 3 current vectors, a combined plot of the total induced energy CDFs is shown in Fig. 4.9. Comparing with the results in Fig. 4.4, 4.5, 4.6 and 4.7, the probability of receiving zero energy at 1 m is lower than using constant current but higher than using 8 or more current vectors. At 0.5 m, the performance is similar to using more current vectors. Thus, if the wireless energy transfer range is long, i.e., around 1 m, it is more reliable to use more than 8 current vectors. On the contrary, if the range is short, i.e., around 0.5 m, it is sufficient to use 3 current vectors.

Numerical simulations therefore suggest the feasibility of our proposed algorithm with a number of current vectors ranging from a minimum of 3 mutually perpendicular directions to a maximum of 32 current vectors. The more correlation between consecutive current vectors is confirmed and visible in the charging profile diagrams as the number of current vectors increases. Moreover, the CDF of total energy received in a charging cycle compares the effectiveness of current sets of varying sizes in charging a large number of randomly oriented receivers in space. We observe a higher probability of obtaining less than the minimal amount of energy (1mJ) for smaller current sets, the highest being for a constant current (1 current vector). However, this same current set obtains the highest possible energy received in a charging cycle due to the fact that a receiver will receive maximum energy throughout a charging cycle once it is optimally aligned with the constant magnetic field, however a changing magnetic field will always have some optimal current vectors for a given sensor, and others may be sub-optimal as the magnetic field covers the three-dimensional space. The constant current set exhibits a higher variance than the optimized current sets, suggesting less reliability. Also, for respective current vectors, the variance increases with distance thereby exhibiting a deterioration in reliability towards the far-field. This confirms the theoretical proof of the range within which induced voltage, and therefore, total energy varies between the near-field and far-field regions.

5 PROOF-OF-CONCEPT IMPLEMENTATION

In order to confirm the practical application of this proposed, and numerically tested algorithm, an experimental implementation and analysis of this system is expedient in an attempt to realize the obtained results in chapter 4. In this section, we outline the methodology that was employed and the results thereof. The proof-of-concept consists of two main blocks, a transmitter and receiver. The final transmitter block is shown in Fig. 5.3.

5.0.1 Signal Generation

The end goal was to supply a sinusoidal voltage signal to each coil of the tri-axis coil array in order to provide them with their respective currents as required by a particular current. With knowledge of the coil impedance, we could control the current supplied by controlling the amplitude of the supplied voltage. A 100 MHz Nexys4 FPGA board is used to generate and control a PWM that is used to control the transmitter supply voltage and frequency. The 100 MHz clock frequency enables us to produce a 10 MHz signal, since the rated frequency can be stepped down by a whole number of 10 to achieve this frequency, which is challenging to do for a target frequency of 13.56 MHz.

Amplitude and Frequency Control

In order to provide amplitude control, a pulse width modulated wave (PWM) is supplied from the FPGA. By modulating the duty cycle of the wave, we can accordingly change the average voltage level which determines the amplitude of the supplied voltage. We can then change the current supplied to each tri-axis coil based on the calculated values for the desired alignment of the resultant magnetic field.

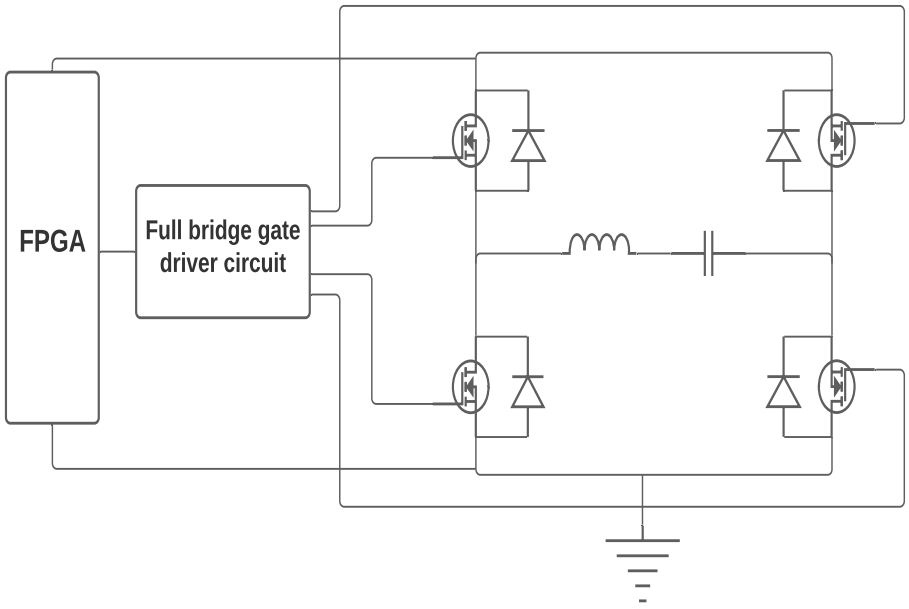

FIGURE 5.1: Date driver-based signal generator

We aim to synchronize the communicating frequency with the resonance frequency of the tri-axis coils. This will be determined by the frequency at which we drive the MOSFETs in the amplifier circuit. At high frequencies in the MHz range, square waves used to generate switching signals are very susceptible to noise, and the unclean signal can result in spurious switching of MOSFETs. In order to obtain a reliable square wave to drive transistors, two methods were studied into detail.

- **Comparator-based direct MOSFET switching.** In this first method, the signals that drive the MOSFET gates are first passed through a comparator circuit with a reference voltage at 50% the amplitude of the signal. This will ensure that the gate-driving pulse assumes two distinct states as desired. Based on the noise level of the input, the reference voltage can be adjusted to accommodate the anomaly. It must be noted that a direct connection using this method comes with some caveats. The high side MOSFETs have their source connected to the load, and the $V_s = V_l$ where V_s is the source voltage and V_l is the voltage across the load.(the coil in this case) To properly switch a MOSFET on, $V_{gs} > V_{th}$ i.e.,

$$V_g - V_s > V_{th}$$

$$V_g > V_{th} + V_s$$

This necessitates a higher driving gate voltage in order to properly switch on the upper side MOSFET by compensating for the source voltage. In the on state, the MOSFET acts as a resistor of very low resistance and forms a voltage divider with the low side MOSFET and the load impedance as shown in Fig. 5.2. It can be seen that:

$$V_s = V_{cc} \times \frac{R_{\text{load}} + R_{\text{low}}}{R_{\text{load}} + R_{\text{low}} + R_{\text{high}}},$$

where

- R_{low} = On resistance of low side MOSFET
- R_{high} = On resistance of high side MOSFET
- R_{load} = Load resistance
- V_{cc} = Supply voltage from FPGA

$$R_{\text{load}} >> R_{\text{high}} = R_{\text{low}}$$

$$V_s \approx V_{cc}$$

To properly switch a high side MOSFET, $V_g \approx V_{cc} + V_{th}$.

The pulsed nature of the MOSFET input to be used to control the amplitude of the sinusoidal wave will make a direct switching of the high side MOSFET challenging.

- **Integrated MOSFET Gate Driver Circuit.** Full-bridge MOSFET gate driver circuits are specifically designed to deal with the outlined challenge that is

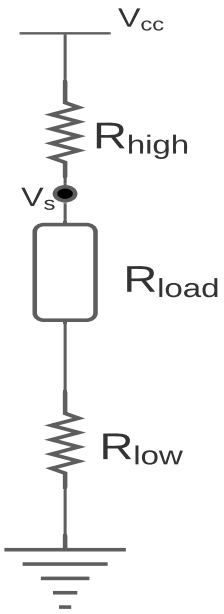

FIGURE 5.2: Effective circuit of bridge inverter

concomitant with the comparator-based methodology. These circuits effectuate both high-side and low-side switching of MOSFETs an inverter circuit thereby ensuring the complete switching of power MOSFETs that may have high gate voltage requirements. As shown in fig. 5.1, in lieu of the comparator circuit system, an integrated MOSFET-based amplifier with gate drivers is used to provide a more reliable inverter system to supply power to the transmitter.

Prototype Implementation

A proof-of-concept prototype, as shown in Fig. 5.4 is developed. This is an implementation of the final design circuit detailed in Fig. 5.3.

Extensive experimentation and detailed results are presented in the paper "Magnetic Blind Beamforming for Battery-Free Wireless Sensor Networks" which has been submitted to the IEEE transaction on Green Communications and Networking. Here, a MOSFET-based amplifier is employed in controlling the amplitude and phase of the output. Three hand-wound 9-turn square unidirectional coils with 12 cm sides constitute the tri-axis coil. The coils derive their input from three

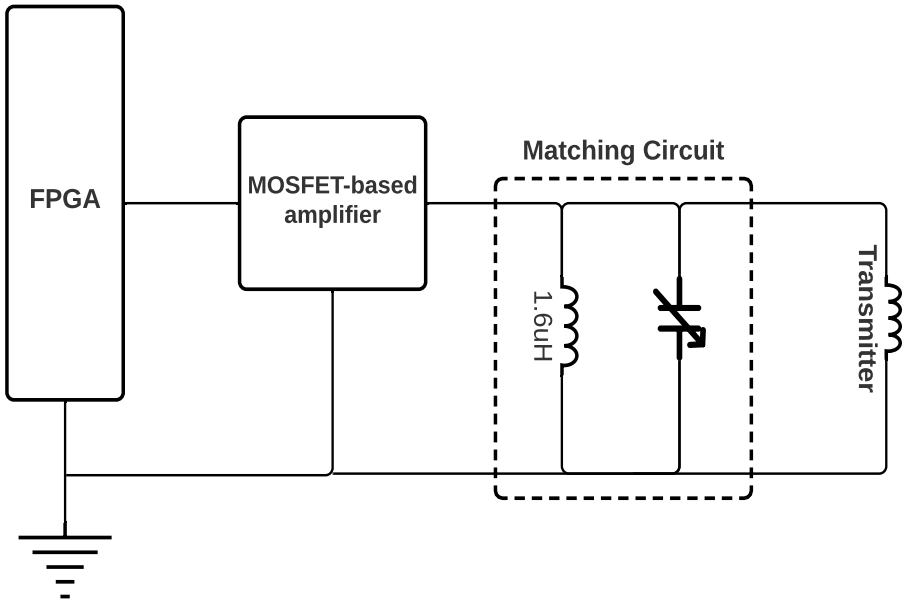

FIGURE 5.3: Signal generation circuit for one coil in the tri-axis transmitter

2EDF7275F development boards from Infineon Technologies are used in this implementation to support the considered operating frequency of 10 MHz *Infineon 2EDF7275F DataSheet*. A variable capacitor and 1.6 μH inductor are introduced as a matching circuit which sits between the development board and transmitter coil. This effectuates the reduction of reactive impedance thereby rendering the transmitter circuit predominantly resistive. The current supplied to the tri-axis coils can then be reliably controlled by manipulating the voltage since the current is directly proportional to the voltage in this resonant state.

The feasibility of the magBB algorithm is validated in this paper by comparing measured results to the expected performance suggested by the simulated values in this study. 7 current vectors are developed based on the MagBB algorithm and the performance of these vectors is compared with that of a mutually orthogonal set of current vectors and a constant current set at a radial distance of 10 cm and 20 cm from a 2.5 cm radius receiver coil. The blind beamforming vectors are confirmed to adequately deliver power to the receiver coil with better higher reliability than a constant current set.

The presented results suggest that a range of 30 cm can be obtained within which

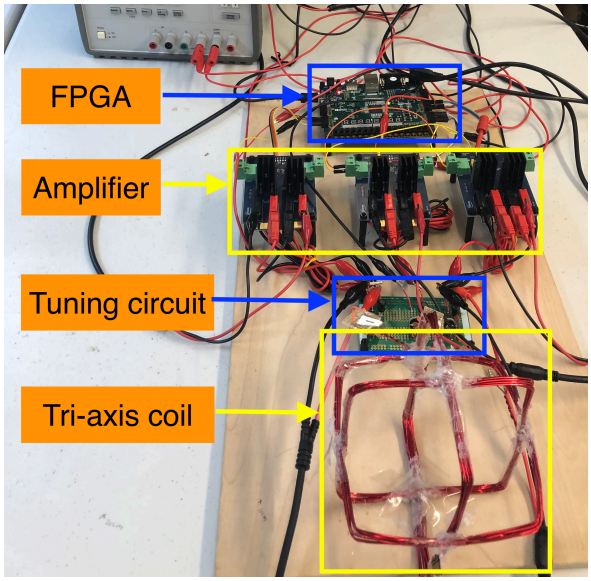

FIGURE 5.4: The developed proof-of-concept prototype.

induced voltages above 100 mV are observed. Since the proposed application discussed is for wireless charging for underground sensors, the transmission power can be increased to boost the received power and range. Also, the efficiency of the system can be improved by using more integrated circuits to eliminated leakage due to cables, and eliminating non-linearities with perfectly matched coils.

6 CONCLUSIONS

A magnetic blind beamforming (MagBB) algorithm has been proposed in this study to wirelessly charge batteryless sensors with unknown coil orientations. The efficiency of magnetic induction-based wireless energy transfer strongly depends on the coil alignment. The misalignment causes significant losses. Since batteryless sensors use diodes in the energy harvesting circuit, if the induced voltage is lower than the diode threshold voltage, no energy can be received. MagBB can rotate the magnetic fields at a point which can ensure that part of the magnetic fields can be leveraged to charge a sensor. So far, this research has provided a detailed design procedure for MagBB and has discussed its reliability, location dependency, and efficiency. Extensive simulations have been performed to evaluate the performance of MagBB. A proof-of-concept prototype was designed whose practical performance has been validated by experimentation in subsequent studies. The results suggest that MagBB can effectively charge sensors without knowing their coil orientation. This can enable the use of large numbers of tiny batteryless sensors for applications such as precision agriculture and structural health monitoring.

BIBLIOGRAPHY

Balanis, Constantine A (2016). *Antenna theory: analysis and design*. John wiley & sons.

Chen, Shaoyuan et al. (2016). "A multiantenna RFID reader with blind adaptive beamforming". In: *IEEE Internet of Things Journal* 3.6, pp. 986–996.

Dong, Xin, Mehmet C Vuran, and Suat Irmak (2013). "Autonomous precision agriculture through integration of wireless underground sensor networks with center pivot irrigation systems". In: *Ad Hoc Networks* 11.7, pp. 1975–1987.

Guo, H. and Z. Sun (2014). "Channel and Energy Modeling for Self-Contained Wireless Sensor Networks in Oil Reservoirs". In: *IEEE Transactions on Wireless Communications* 13.4, pp. 2258–2269. DOI: 10.1109/TWC.2013.031314.130835.

Guo, H., Z. Sun, and P. Wang (2015a). "Channel Modeling of MI Underwater Communication Using Tri-Directional Coil Antenna". In: *2015 IEEE Global Communications Conference (GLOBECOM)*, pp. 1–6. DOI: 10.1109/GLOCOM.2015.7417399.

— (2015b). "Channel Modeling of MI Underwater Communication Using Tri-Directional Coil Antenna". In: *2015 IEEE Global Communications Conference (GLOBECOM)*, pp. 1–6.

Guo, Hongzhi (2020). "Performance Analysis of Near-Field Magnetic Induction Communication in Extreme Environments". In: *Progress In Electromagnetics Research Letters* 90, pp. 77–83.

Guo, Hongzhi, Zhi Sun, and Pu Wang (2017). "Multiple frequency band channel modeling and analysis for magnetic induction communication in practical underwater environments". In: *IEEE Transactions on Vehicular Technology* 66.8, pp. 6619–6632.

Infineon 2EDF7275F DataSheet. URL: https://www.infineon.com/dgdl/Infineon-2EDF7275F-DataSheet-v02_07-EN.pdf?fileId=5546d462636cc8fb0163b08fd9203057.

Jadidian, Jouya and Dina Katabi (2014). "Magnetic MIMO: how to charge your phone in your pocket". In: *MobiCom '14*.

Kisseleff, Steven, Ian F Akyildiz, and Wolfgang H Gerstacker (2014). "Throughput of the magnetic induction based wireless underground sensor networks: Key optimization techniques". In: *IEEE Transactions on Communications* 62.12, pp. 4426–4439.

Luo, Z. et al. (2010). "Semidefinite Relaxation of Quadratic Optimization Problems". In: *IEEE Signal Processing Magazine* 27.3, pp. 20–34.

Ma, Yunfei et al. (2018). "Enabling Deep-Tissue Networking for Miniature Medical Devices". In: *Proceedings of the 2018 Conference of the ACM Special Interest Group on Data Communication*. SIGCOMM '18. Budapest, Hungary: Association for Computing Machinery, 417–431. ISBN: 9781450355674.

Maselli, Gaia et al. (2019). "Battery-Free Smart Objects Based on RFID Backscattering". In: *IEEE Internet of Things Magazine* 2.3, pp. 32–36.

Matsur, I. Y. et al. (2017). "On designing an underground induction antenna for vehicle identification". In: *2017 IEEE International Conference on RFID Technology Application (RFID-TA)*, pp. 266–271. DOI: 10.1109/RFID-TA.2017.8098897.

Morag, Yahav et al. (2019). "Channel Capacity of Magnetic Communication in a General Medium Incorporating Full-Wave Analysis and High-Frequency Effects". In: *IEEE Transactions on Antennas and Propagation* 67.6, pp. 4104–4118.

Ofori, Albert Aninagyei and Hongzhi Guo (2021). "MagBB: Wireless Charging for Batteryless Sensors Using Magnetic Blind Beamforming". In: *2021 IEEE 18th Annual Consumer Communications Networking Conference (CCNC)*, pp. 1–8. DOI: 10.1109/CCNC49032.2021.9369529.

Sun, Z. and I. F. Akyildiz (2010). "Magnetic Induction Communications for Wireless Underground Sensor Networks". In: *IEEE Transactions on Antennas and Propagation* 58.7, pp. 2426–2435. DOI: 10.1109/TAP.2010.2048858.

Tan, X., Z. Sun, and I. F. Akyildiz (2015). "Wireless Underground Sensor Networks: MI-based communication systems for underground applications." In: *IEEE Antennas and Propagation Magazine* 57.4, pp. 74–87. DOI: 10.1109/MAP.2015.2453917.

Vuran, Mehmet C et al. (2018). "Internet of underground things in precision agriculture: Architecture and technology aspects". In: *Ad Hoc Networks* 81, pp. 160–173.

Yang, Gang, Mohammad R Vedady Moghadam, and Rui Zhang (2017). "Magnetic MIMO signal processing and optimization for wireless power transfer". In: *IEEE Transactions on Signal Processing* 65.11, pp. 2860–2874.

Yedavalli, Pavan S et al. (2017). "Far-field RF wireless power transfer with blind adaptive beamforming for Internet of Things devices". In: *IEEE Access* 5, pp. 1743–1752.

Zhao, Renjie et al. (2020). "NFC+ Breaking NFC Networking Limits through Resonance Engineering". In: *Proceedings of the Annual conference of the ACM Special Interest Group on Data Communication on the applications, technologies, architectures, and protocols for computer communication*, pp. 694–707.